AIAA JOURNAL
Vol. 45, No. 7, July 2007

Aero-Optical Interactions Along Laser Beam Propagation Paths in Compressible Turbulence

Fazlul R. Zubair* and Haris J. Catrakis†
University of California, Irvine,
Irvine, California 92697-3975

DOI: 10.2514/1.27342

Aero-optical interactions along laser beam propagation paths in turbulent compressible separated shear layers are examined on the basis of experiments on direct imaging of the refractive-index field. Imaging of the index-of-refraction field is performed using digital photography techniques with laser-induced fluorescence. A pulsed ultraviolet laser sheet is directed through the shear layer to generate the fluorescence by exciting acetone vapor molecularly mixed with air in the freestream, resulting in light in the visible spectrum that is recorded with a high-resolution digital camera system. We introduce the idea of the interaction optical path difference and its associated rms value ($IOPD_{rms}$), and we investigate these quantities as functions of propagation distance along the laser beam direction as well as functions of the laser aperture size. Evidence of nonmonotonic behavior of the $IOPD_{rms}$ as a function of propagation distance in the flow is observed for individual realizations. The relative magnitude of this nonmonotonic behavior depends on the laser aperture size in relation to the large scales of the flow. These observations of nonmonotonic behavior suggest the presence of a turbulence-induced mechanism for partial reductions in the beam aberrations, which is related to physical and geometrical properties of high-gradient refractive-index turbulent interfaces.

I. Introduction

AERO-OPTICS, as discussed in recent review articles [1,2], presents several challenges both fundamentally and in applications. One of the basic goals is to physically relate the behavior of turbulence-generated refractive-index fields to the structure of turbulence-distorted optical wave fronts. Following the pioneering work in the field of aero-optics by Liepmann [3], advances in the understanding of turbulence and its aero-optical effects continue to be pursued theoretically, experimentally, and computationally [4–9]. Knowledge of the aero-optical interactions and identification of the dominant flow mechanisms in the generation of aero-optical distortions are needed in both basic and applied problems in aero-optics [1]. Applied challenges include airborne directed-energy applications such as communications and defense systems. In addition, understanding of aero-optical properties is useful as a means of developing optical methods for probing the behavior of large Reynolds number flows in the laboratory, in the field, or remotely [10].

The basic physical interactions between the propagating optical wave fronts and the aberrating turbulent flows occur across the refractive-fluid interfaces. Thus, an improved understanding of the interfacial behavior is needed [2]. At large Reynolds numbers, however, the refractive interfaces are highly irregular and extend over a wide range of scales. Thus, experiments at large Reynolds numbers are particularly desirable because they complement computational studies and physical modeling. This is because direct numerical simulations are presently limited in terms of the Reynolds numbers that can be explored [11], and large-eddy simulations can be sensitive to subgrid-scale modeling [7,12]. Furthermore, one would like also to incorporate compressibility effects and flow geometry effects on the modeling of the large Reynolds number behavior. Previous work in aero-optics includes studies of the large-scale properties [5,8,9,13] and small-scale properties [7,14,15]. The available studies agree that the near-field aero-optical effects in turbulent shear flows are mainly caused by the large-scale flow structures [8,9]. In addition, knowledge of the large-scale aero-optical behavior can be useful regarding modeling of the cumulative contributions of the small scales relative to the large scales. This is especially important for problems involving long-range optical beam propagation through atmospheric turbulence [14].

In the present work, the aero-optical interactions along laser beam propagation paths are analyzed in high Reynolds number separated compressible shear layers. In the following section, the variable-pressure flow facility at the University of California, Irvine is described, which is used to generate and image the turbulent compressible shear layers. The freestream, which consists of air seeded with a low concentration of acetone vapor, is directed into the test section, which is contained within a pressure vessel filled with ambient air. Direct imaging of the refractive-index field and interfaces is conducted using a technique known as laser-induced fluorescence in combination with digital photography. An ultraviolet laser sheet excites the acetone vapor, which fluoresces in the visible spectrum. This fluorescence is recorded with a high-speed digital camera system. This enables recording of high-quality two-dimensional spatial images of the refractive-index field, which are presented in Sec. III. The Reynolds number based on the visual thickness of the flowfield is $Re \sim 6 \times 10^6$ and the convective Mach number is $M_c \sim 0.4$. The refractive-index fields are analyzed to identify the refractive interfaces and used to investigate the wave front behavior. We introduce the interaction optical path difference (IOPD) and we examine its rms value ($IOPD_{rms}$) using the refractive fields. These results, shown in Sec. III, demonstrate nonmonotonic behavior of the laser wave front as it propagates through the shear layer. Analysis of the refractive-index field and aero-optical effects indicates that the nonmonotonic behavior (i.e., the partial reductions in the $IOPD_{rms}$) are the result of interactions that occur across the locally thin high-gradient interfaces. We present examples of this turbulence-induced mechanism, and we examine the effect of hypothetical laser aperture size. In the Conclusions in Sec. IV, implications of the present findings are discussed.

Presented as Paper 3070 at the 37th Plasmadynamics and Lasers Conference, San Francisco, CA, 5–8 June 2006; received 17 August 2006; accepted for publication 14 January 2007.

*Graduate Student, Mechanical and Aerospace Engineering; fazlul.zubair@uci.edu. Member AIAA.

†Associate Professor, Mechanical and Aerospace Engineering; catrakis@uci.edu. Member AIAA (Corresponding Author).

II. Flow Facility, Experiments, and Computations

A. Experimental Technique

The aero-optics variable-pressure flow facility used in the present investigations can be seen in the photograph in Fig. 1. This facility allows experiments to be conducted at elevated test section pressures, in the range $15 \lesssim p \lesssim 300$ psi ($1 \lesssim p \lesssim 20$ atm), which allow higher signal-to-noise ratio flow imaging than would be possible at atmospheric or subatmospheric pressures. For imaging techniques based on laser-induced fluorescence, such as the method presently used and described in this section, the resulting image signal-to-noise ratio is sufficiently high to enable an interface-based examination of the aero-optical interactions. This is due to the increased local density of air molecules as a result of conducting the experiment at higher operating pressures.

The laboratory facility primarily consists of a blowdown wind tunnel contained inside a large variable-pressure vessel. The main aero-optics vessel, in which the wind tunnel is housed, is oriented upright and is shown on the right in Fig. 1. The gas reservoir, which supplies fluid to the wind tunnel, is oriented horizontally and is shown on the left in Fig. 1. The maximum supply pressure of the reservoir is $\sim 3,000$ psi or ~ 200 atm. The maximum operating pressure of the aero-optics vessel is ~ 300 psi or ~ 20 atm. The main vessel is ~ 2.44 m (~ 8 ft) in height and ~ 1.22 m (~ 4 ft) in diameter, enabling up to two people to stand in the interior when reconfiguring the test section or the tunnel. The main vessel has a quick-release entrance door of $\sim .61$ m (~ 2 ft) in diameter that facilitates access in and out of the vessel. Both the main pressure vessel and the reservoir vessel are ASME U-Stamp rated. Two ellipsoidal cap sections for each vessel are welded at the two ends of the main cylindrical sections. Both vessels, including the quick-release door mechanism, were fabricated by Melco Steel. The main vessel and the reservoir vessel are equipped with National Pipe Thread (NPT) fittings for attachments of pressure gauges, vacuum lines, transducers, and any other instrumentation necessary for flow management.

Extensive optical access to the interior of the main pressure vessel is available through five high-optical-quality spectrosil windows, each with a diameter of 25 cm (10 in.) and a thickness 8.32 cm (3.25 in.). Four of the five windows are vertical optical ports located on the four sides of the main pressure vessel. The fifth window is a horizontal optical port located on the top of the vessel. Combined with laser diagnostics, this facility is capable of quantitative high-resolution imaging of high Reynolds number compressible turbulent flowfields.

Fig. 2 Schematic showing the separated shear-layer geometry. The larger rectangular box indicates the extent of the shadowgraphs of the shear layer and the smaller square box indicates the part of the shear layer imaged.

The flow geometry currently examined is a separated turbulent shear layer (see Figs. 2 and 3) that is an example of a separated flow relevant in a wide range of contexts [16] including aero-optics problems [4]. In the laboratory experiments, the flow is directed vertically upward through the pressure vessel and the beam propagation is horizontal. The separated shear layer represents a basic flow configuration of interest for future studies in which more complex flow geometries can be observed. For example, although separated flows over curved surfaces have an unsteady separation point, the sharp 90-deg corner defined in the present flow geometry ensures a fixed separation point. Studies of the unforced separated shear layer can provide valuable baseline information to evaluate the extent to which active flow control techniques, including large-scale disorganization or regularization, can be effective [1,17].

In the present studies, acetone vapor molecularly mixed in air is used. To generate the purely gaseous air/acetone mixture, a stream of air is passed through a liquid bath of acetone using the bubbling method [18]. The air/acetone mixture is supplied to the reservoir,

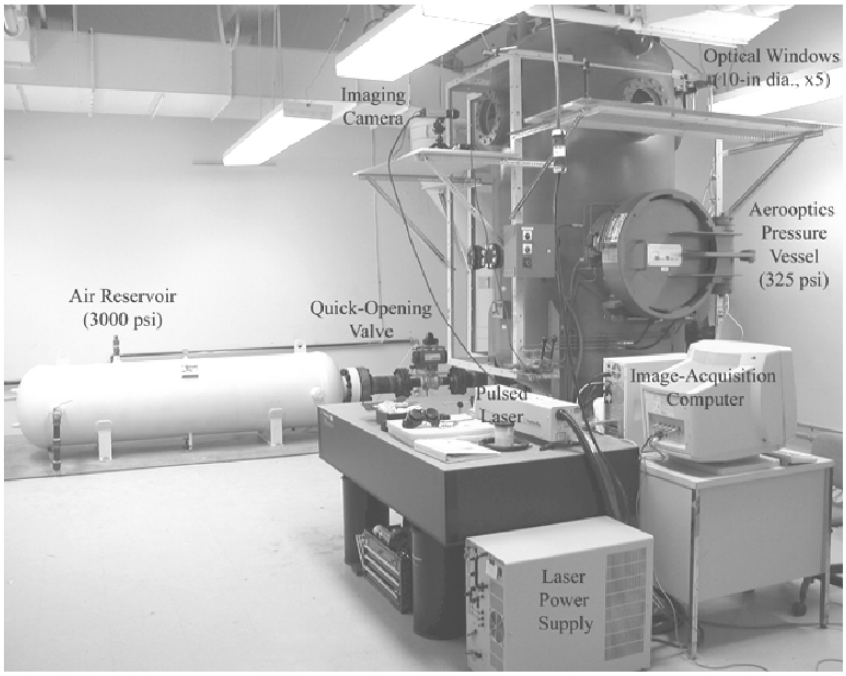

Fig. 1 Photograph of the aero-optics variable-pressure flow facility at the University of California, Irvine. The main pressure vessel is visible in the right part of the photograph. It has a large interior and cross section, extensive optical access, and a quick-release door to facilitate investigations of aero-optical phenomena at variable pressures. Combined with laser and imaging diagnostics, this facility enables high-resolution flow imaging and beam measurements of aero-optical flows at large Reynolds numbers with compressibility effects. The blowdown wind tunnel and test section are housed inside the main vessel.

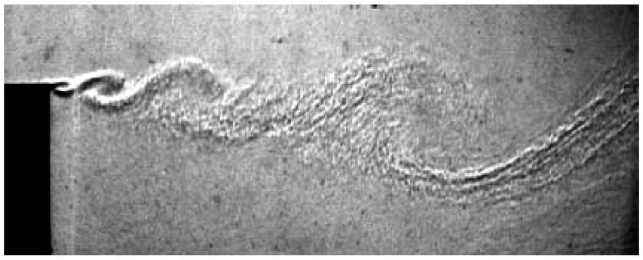

Fig. 3 Example of a shadowgraph of the compressible turbulent separated shear layer.

which is pressurized before each experimental run. The main vessel is pressurized with filtered air to $p \sim 45$ psi ($p \sim 3$ atm) before releasing the reservoir gas into the blowdown tunnel and test section. The acetone-vapor concentration in air is regulated by controlling the mass flux of air through the bubbling unit. In the present experiments, an acetone-vapor concentration of $\sim$2% by volume is generated to ensure negligible absorption of the laser energy, similar to previous experiments on laser-induced fluorescence [19], and to maintain conditions below the lower flammability limit of acetone. At the conclusion of each run, fresh filtered air is pumped into the main and reservoir vessels, and the system is flushed several times before setting up another experiment. This ensures that we are able to control the acetone concentration in the reservoir vessel as well as sufficiently flush any ambient acetone out of the main vessel.

The ultraviolet beam used in the present study is generated from a pulsed Nd:YAG laser. The illumination source employed is a moderate-energy laser system (Spectra Physics model INDI 40-10) that produces $\sim$70 mJ ultraviolet light pulses at a wavelength of 266 nm. This wavelength corresponds to frequency quadrupling at the fourth harmonic of the illumination sources fundamental infrared 1064-nm output. The laser beam is shaped into a laser sheet with a width of $\sim$15 cm and a thickness of $\sim$150 μm using a cylindrical lens. A parabolic mirror ensures that the laser sheet that is produced from the lens is of parallel extent before it propagates through the test section. The laser sheet is directed through the quartz windows of the pressure vessel and into the high Reynolds number separated shear layer. The laser-sheet orientation corresponds to a streamwise slice of the turbulent shear layer. The extent of the laser sheet that illuminates the shear layer is approximately $\sim 15 \times 15$ cm. The laser-sheet width of $\sim$15 cm corresponds to the downstream extent of the imaged flowfield. The large-scale transverse extent of the shear layer at the imaging location is approximately $L \sim 10$ cm. The incident laser sheet excites the acetone vapor in the air to generate visible (blue) light through fluorescence. The elevated test section pressure of $p \sim 45$ psi ($p \sim 3$ atm) results in a significant increase in the fluorescence signal, relative to atmospheric or subatmospheric test section pressures, in agreement with previous studies [18].

The laser-induced fluorescence signal is recorded on a high-resolution digital intensified charge-coupled device (ICCD) camera with $\sim 1000^2$ pixels, examples of which can be seen in Figs. 4 and 5. The camera system is oriented along a direction normal to the incident laser sheet and, therefore, perpendicular to the laser propagation direction. The digital camera system employed is an ICCD camera by Stanford Photonics (Mega-10Z) with enhanced sensitivity in the blue visible spectrum. This enables the recording of the two-dimensional spatial slices of the acetone-vapor-concentration field in the turbulent shear layer with a high signal-to-noise ratio, estimated at approximately 100:1, which is large enough to accurately identify and extract refractive-index interfaces. The fluorescence-signal images are normalized and calibrated pixel by pixel using post-run images recorded at uniform concentration as well as prerun images that correspond to pure air images in the test section. The normalization and calibration procedure has been described in a previous study [19]. The experiments are conducted at a sufficiently low acetone concentration and laser energy so that the intensity of the fluorescence is linearly related to the concentration of acetone in the local mixture. In the present experiments, the compressible turbulent mixing of the freestream gas, which itself

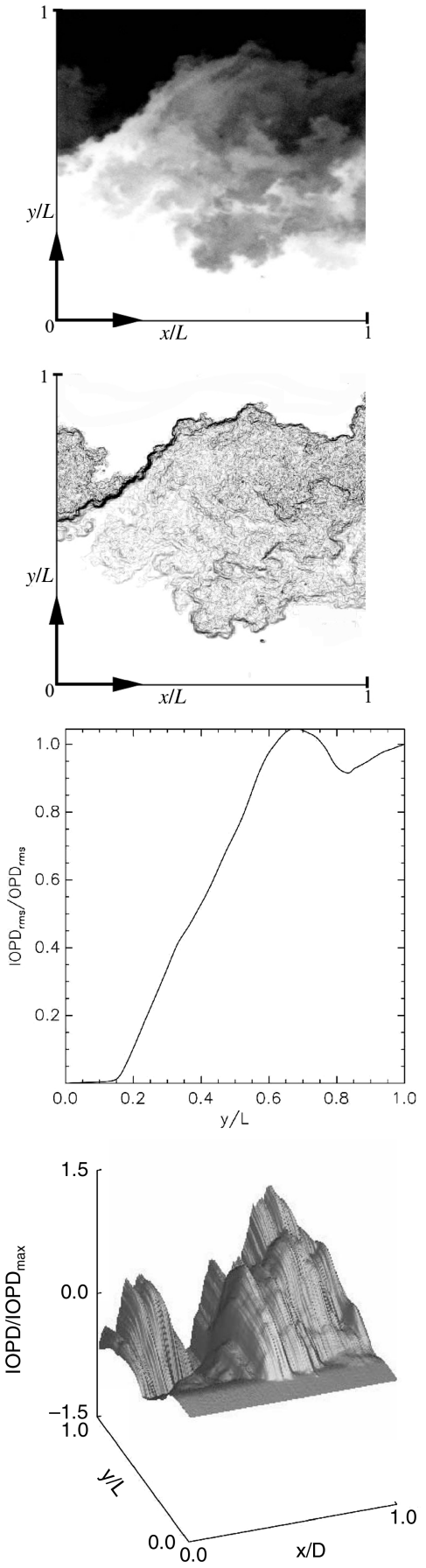

Fig. 4 Example of laser-induced florescence image of a separated shear layer with associated refractive-index interfaces. Plots depicting the IOPD$_{rms}$ and IOPD surfaces of the corresponding image are also shown. In this case, $D = L$, corresponding to a full-width image.

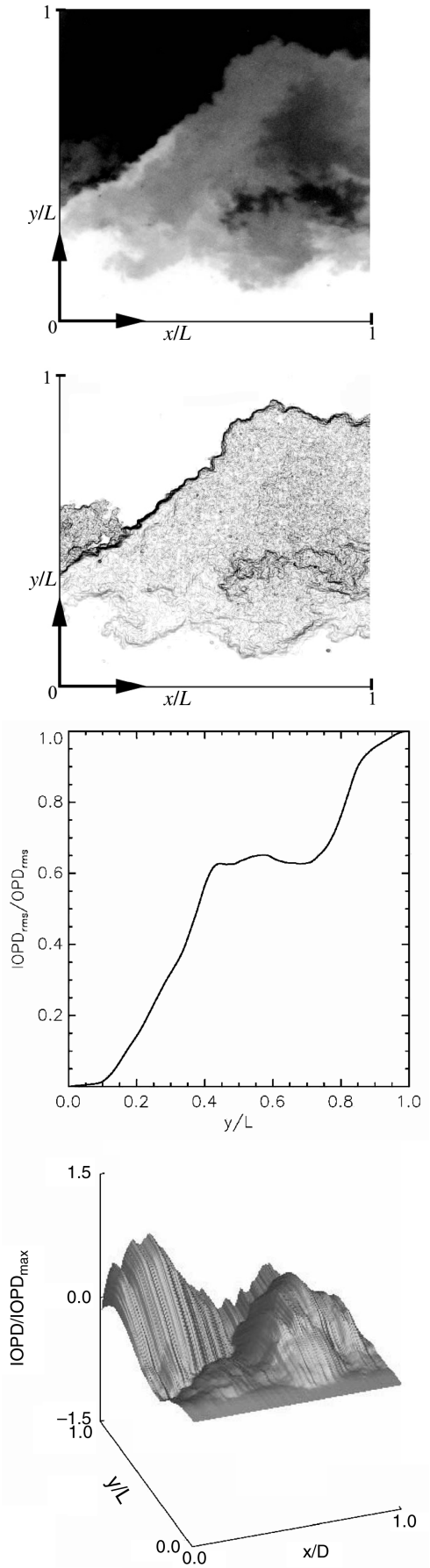

Fig. 5 Example of laser-induced florescence image of a separated shear layer with the associated refractive-index interfaces. Plots depicting the $\mathrm{IOPD_{rms}}$ and IOPD surfaces of the corresponding image are also shown. In this case $D = L$ corresponding to a full-width image.

contains a mixture of acetone and air, with the ambient pure air generates the acetone-vapor-concentration field, which corresponds directly to the refractive-index field. The intensity of the fluorescence thus yields the local concentration of acetone, which represents the magnitude of the index-of-refraction change caused by the freestream air and its interaction with the stagnant pure air in the test section. In addition, because of the low concentration of acetone employed, there is no significant beam steering observed in these images. Significant beam steering would result in intensity streaks in the images (as occurred, for example, in a previous different study [5]), which are absent in the laser-induced fluorescence images generated in these experiments.

B. Computational Techniques

Knowledge of the refractive-index field is useful for evaluating the optical wave front distortions and for identifying the dominant fluid

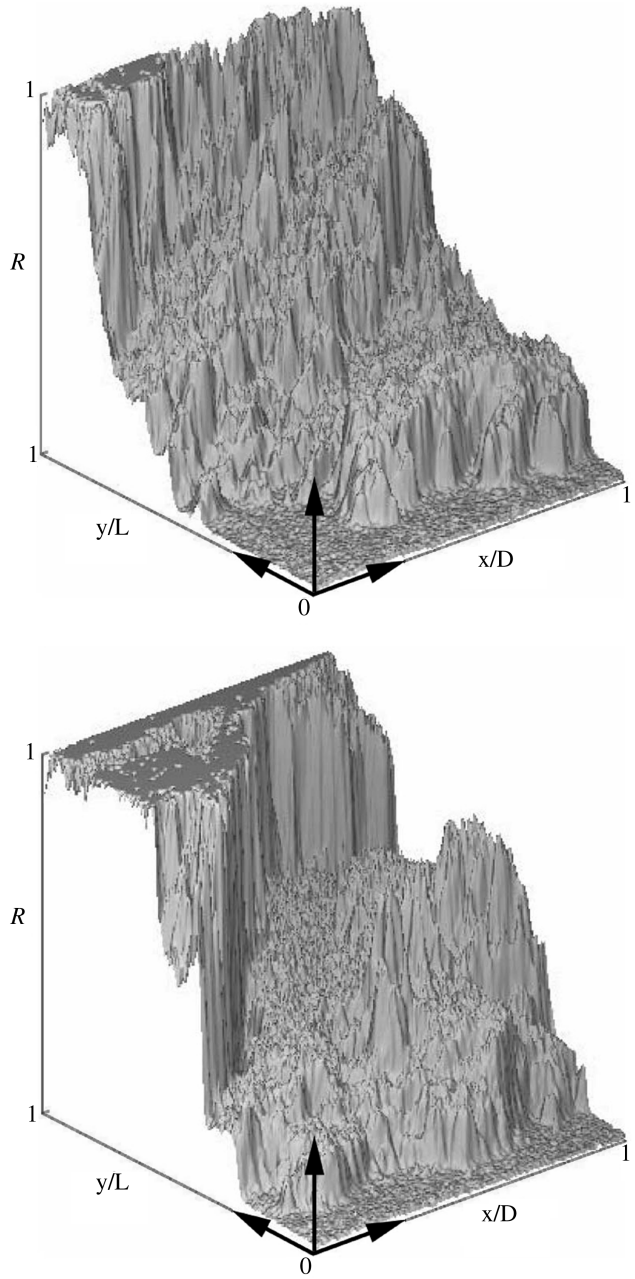

Fig. 6 Surface plots depicting the refractive-index variations in the laser-induced florescence images shown in Figs. 4 and 5. The top plot corresponds to Fig. 4 and the bottom plot corresponds to Fig. 5. R is defined as $[n(x,y) - n_0]/(n_L - n_0)$, where n_0 is the x-averaged refractive index at $y/L = 0$ and n_L is the x-averaged refractive index at $y/L = 1$.

a) b)

Fig. 7 Two partial images of turbulent shear layers. Each image was derived from an image of a full turbulent shear layer, assuming the laser propagated into the shear layer had an aperture half the size of the actual beam ($D = L/2$).

interfaces in the aero-optical interactions [5,8]. Examples of the resulting wave front distortions, associated with the interactions across the refractive-index interfaces, are shown in Figs. 4 and 5. The present work only addresses near-field interactions, which are sufficiently well described by geometrical optics, whereas far-field interactions would require the use of wave descriptions based on Maxwell's equations [6,20]. For high-energy laser airborne applications and far-field propagation, one would have to consider the two-way coupling between the turbulent field and the optical waves for far-field propagation, whereas for low-energy beams, there is only one-way coupling between the flow structure and the beam distortion [5,21,22].

For the present studies, the measured refractive-index fields are used with the eikonal equation of geometrical optics to computationally propagate the optical wave fronts in the near field. Because the smallest turbulent scales are greater than the optical wavelength scales [23], the geometrical-optics description is sufficient for the near-field interactions. In terms of the refractive-index field n and the optical path length (OPL), the eikonal equation is [24]

$$|\nabla(\mathrm{OPL})| = n \tag{1}$$

Solutions of this equation, by inverting and integrating along the entire individual ray paths, correspond to the total OPL integral in terms of the refractive-index field, which can also be expressed as a total integral in terms of the local thickness of the refractive interfaces [9]. To study the aero-optical interactions (i.e., the behavior at each location in the flow encountered by the laser beam along its path), we introduce the interaction optical path length (IOPL), which we define as the running-integral version of the OPL but with a running integral of the refractive field (i.e., as a function of the partial distance along the laser path throughout the turbulent field), as follows:

$$\mathrm{IOPL}\,(\ell, t) \equiv \int_{\ell_0}^{\ell} n(\ell', t)\mathrm{d}\ell' = \int_{\mathrm{path}} n(\ell', t) h_{n,\ell'}(\ell', t)|\mathrm{d}n| \tag{2}$$

where $h_{n,\ell'}(\ell', t)$ is the inverse refractive-index gradient magnitude component in the direction of optical propagation or, equivalently, the refractive interfacial thickness component per unit refractive index:

$$h_{n,\ell'}(\ell', t) = \frac{1}{|\nabla n(\ell', t)|_{\ell'}} = \frac{\mathrm{d}\ell'}{|\mathrm{d}n|} \tag{3}$$

as has been shown in the interfacial-fluid-thickness approach in previous work [9].

The IOPL integral corresponds to inverting the eikonal Eq. (1). The physical distance along the beam propagation path for each light ray is denoted as ℓ. It is essential to appreciate that knowledge of the fully integrated information alone (e.g., the total OPL) is, in general, not enough to uniquely identify the aero-optical interactions because of the integration. However, knowledge of the refractive-index field or of the IOPL enables the study of the interactions.

The isosurfaces of the IOPL correspond to the propagating optical wave fronts (i.e., the optical wave fronts as they interact with the turbulent field):

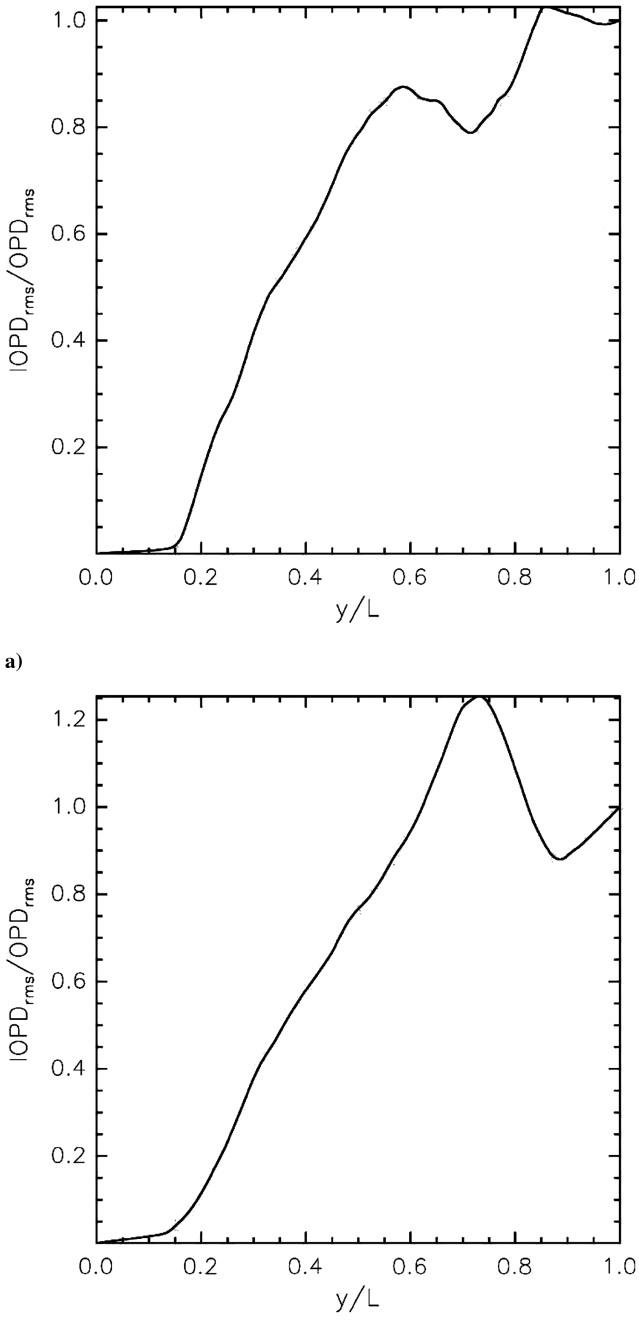

Fig. 8 Associated $\mathrm{IOPD}_{\mathrm{rms}}$ plots of the half-width laser aperture images in Fig. 7.

$$\mathrm{IOPL}\,(\mathbf{x}, t) = \mathrm{const} \tag{4}$$

just as the isosurfaces of the total OPL correspond to the fully propagated optical wave fronts. The IOPL is also a measure of the optical phase or wave front propagation time [1]. In analogy with the optical path difference (OPD), a useful way to quantify the wave front distortions as they are generated in the flow is to consider the interaction optical path difference, given by

$$\mathrm{IOPD}\,(\ell, t) \equiv \mathrm{IOPL}(\ell, t) - \langle \mathrm{IOPL}(\ell, t)\rangle_{\mathrm{avg}} \tag{5}$$

where $\langle \mathrm{IOPL}(\ell, t)\rangle_{\mathrm{avg}}$ corresponds to the aperture-averaged IOPL value. A useful measure of the wave front distortion is the root-mean-square (rms) value of the IOPD variations, that is,

$$\mathrm{IOPD}_{\mathrm{rms}}(\ell, t) \equiv (\langle |\mathrm{IOPD}(\ell, t)|^2\rangle_{\mathrm{avg}})^{1/2} \tag{6}$$

where $\langle\,\rangle_{\mathrm{avg}}$ denotes aperture averaging. The ensemble-averaged total $\mathrm{OPD}_{\mathrm{rms}}$ value for wave fronts corresponding to the present database of refractive-field images was evaluated by computationally propagating wave fronts using the eikonal Eq. (1) through the measured refractive-index variations.

Independent Shack–Hartmann measurements of the aero-optical aberrations were also conducted and found to result in an ensemble-averaged value of $\mathrm{OPD}_{\mathrm{rms}} \approx 0.2\ \mu$m (i.e., in agreement with the flow-derived value of $\mathrm{OPD}_{\mathrm{rms}}$). The Shack–Hartmann camera was designed and built using commercially available components. The line camera used is a Thorlabs LC1-USB 2.0 3000-pixel linear CCD camera with a custom-made 140-lenslet array made of fused silica. It must be noted that this $\mathrm{OPD}_{\mathrm{rms}}$ is for the present flow conditions and corresponds to mixing of dissimilar gases by virtue of the acetone-vapor seeding in the freestream, which can be different from the case of pure density effects [1]. In general, it can be expected to be a function of Reynolds number, Mach number, flow geometry, and many other parameters. The $\mathrm{OPD}_{\mathrm{rms}}$ value can be used to normalize the IOPD profile for each propagating wave front. Also, this quantity is directly related to a measure of beam attenuation known as the Strehl ratio, which is an important quantity for evaluating the effects of the refractive-index field on the peak intensity of the propagated beam [1,5]. The following section will present examples of laser-induced fluorescence images as well as the corresponding plots derived from computational analysis of these images.

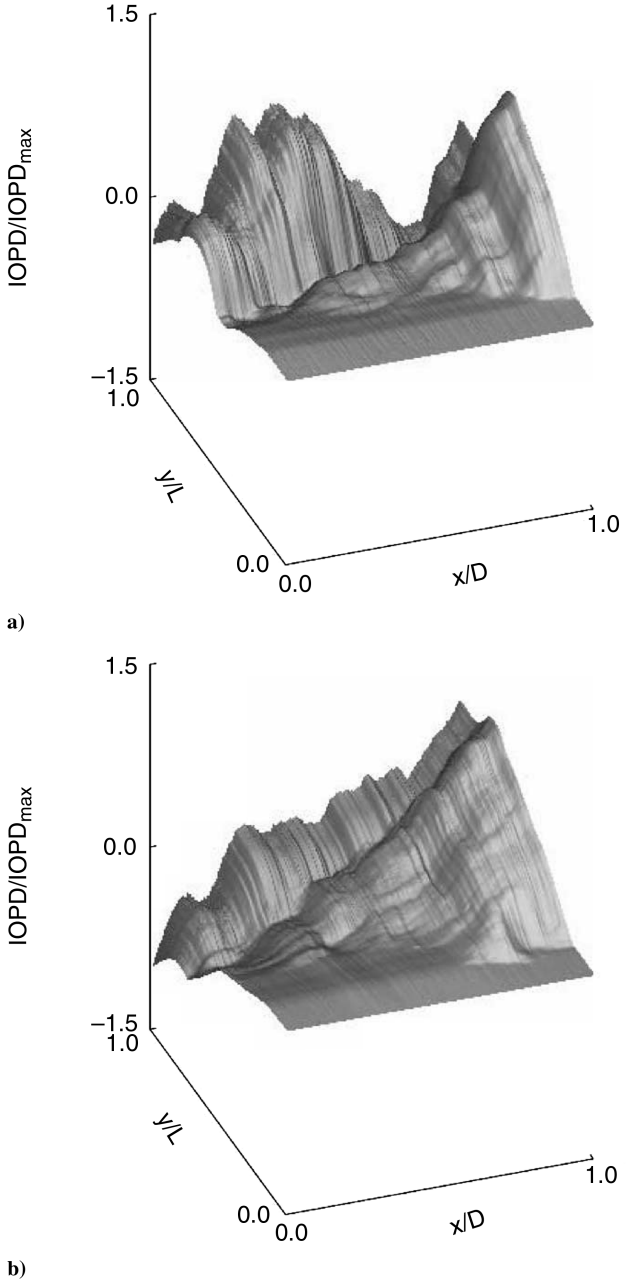

Fig. 9 Associated IOPD surface plots of the half-width laser aperture images in Fig. 7.

III. Experimental and Computational Results

A. Aero-Optical Interactions Along Laser Propagation Paths

The ensemble average of the interaction optical path difference $\mathrm{IOPD}_{\mathrm{rms}}$, calculated using Eq. (6), is a useful measure of the wave front distortion throughout the refractive field. As a laser beam passes through a turbulent field, one might expect that the resulting wave front would become progressively more distorted. However, this may not necessarily be the case as we proceed to investigate. Because the $\mathrm{IOPD}_{\mathrm{rms}}$ is a quantitative measure of how distorted the wave front is, one can compute this value across the entire propagation distance of the laser. The expectation alluded to is that the $\mathrm{IOPD}_{\mathrm{rms}}$ value would monotonically increase as it enters the turbulent field and proceeds to propagate through it, quantitatively showing progressive cumulative distortions of the beam. However, because different parts of a finite aperture laser beam may pass through turbulent interfaces of different structure, this may not necessarily be the case. Using the laser-induced fluorescence images taken with the ICCD camera, a calculation of the $\mathrm{IOPD}_{\mathrm{rms}}$ can be made for laser propagation through

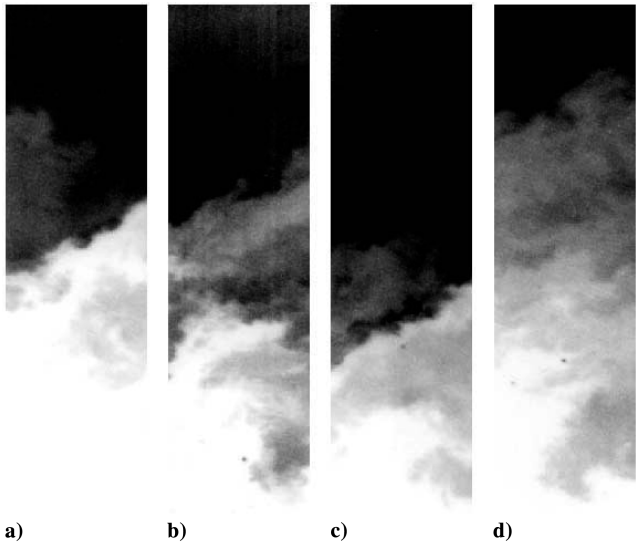

Fig. 10 Four partial images of turbulent shear layers. Each image was derived from an image of a full turbulent shear layer, assuming the laser propagated into the shear layer had an aperture that was a quarter the size of the actual beam ($D = L/4$).

a turbulent shear layer. Figures 4 and 5 show two examples of $IOPD_{rms}$ plots and IOPD surface plots with the associated image of the entire shear layer ($D = L$).

The top images in Figs. 4 and 5 show examples of the turbulent shear layer captured using laser-induced fluorescence. Note that the pure black and white areas in the image represent the freestream and ambient air, respectively. The gray areas represent the mixing field created by the shear layer, which directly relates to the refractive-index field. Below these images are shown the associated refractive gradient fields. Computationally propagating a laser beam through this shear layer allows us to determine the IOPD and $IOPD_{rms}$ along the propagation paths. As expected, the $IOPD_{rms}$ value increases overall as it propagates through the turbulent field. Although as the beam passes through the turbulent shear layer it is frequently distorted further, this increase in distortion is not monotonic, as is indicated in these figures. In Fig. 4, the $IOPD_{rms}$ actually reaches a maximum distortion level after the beam has propagated through ~60% of the flowfield. The beam then becomes partially undistorted until it reaches the ~80% mark and then increases in distortion until it exits the shear layer. Figure 6 (bottom) also shows the corresponding IOPD behavior as a surface plot that, as in the $IOPD_{rms}$ profile, indicates nonmonotonicity in the aero-optical interactions.

In comparison to Fig. 4, Fig. 5 shows a different type of nonmonotonic behavior of the wave front. Initially, we again see an increase of $IOPD_{rms}$ as the beam propagates through the shear layer. Starting at around ~40% of the propagation distance, the $IOPD_{rms}$ appears to level off, with small increases and decreases. At around ~75% of the propagation distance, the $IOPD_{rms}$ increases again till the end of the shear layer. The two examples of images of turbulent separated shear layers produce different $IOPD_{rms}$ profiles. In both cases, we see an increase in the $IOPD_{rms}$ value from the beginning of the shear layer, and in both cases, we see nonmonotonic behavior of the wave front. However, the $IOPD_{rms}$ profile of the wave front is very different in each case. This difference can be attributed to the geometric features of the shear layer. Figure 6 shows surface plots of the refractive-index fields of the images in Figs. 4 and 5. The surface plots serve to visually highlight the refractive-index differences in these two images. Both images start and end with a refractive-index plateau created by the freestream and stagnant air in the pressure vessel, but in between these sections there are different refractive-index changes. The refractive-index fields and the associated $IOPD_{rms}$ profiles suggest that it is the orientation of, and gradients across, the locally thin interfaces that determine the extent of the observed nonmonotonic behavior.

B. Laser Aperture Effects on Aero-Optical Interactions

By computationally propagating wave fronts through the measured shear-layer refractive fields, we proceed to explore the effect of a hypothetical beam aperture size on the nonmonotonic behavior of the wave fronts and its relation to the associated refractive turbulent interfaces. Figure 7 shows parts of two imaged shear layers in which laser beams were computationally propagated. These parts are approximately half the width of the full shear layer ($D = L/2$). Therefore, the aperture size simulated through this computational propagation is comparable to half the aperture size of the beams in Figs. 4 and 5. Figure 8 shows the plots of the $IOPD_{rms}$ value through the half-width shear-layer regions. Nonmonotonic behavior is present in both plots, however, the nature of the profiles differ. In both images, the maximum $IOPD_{rms}$ value does not correlate with the OPD_{rms} value taken at the end of the shear layer. This implies that the wave front reaches a point at which it is more

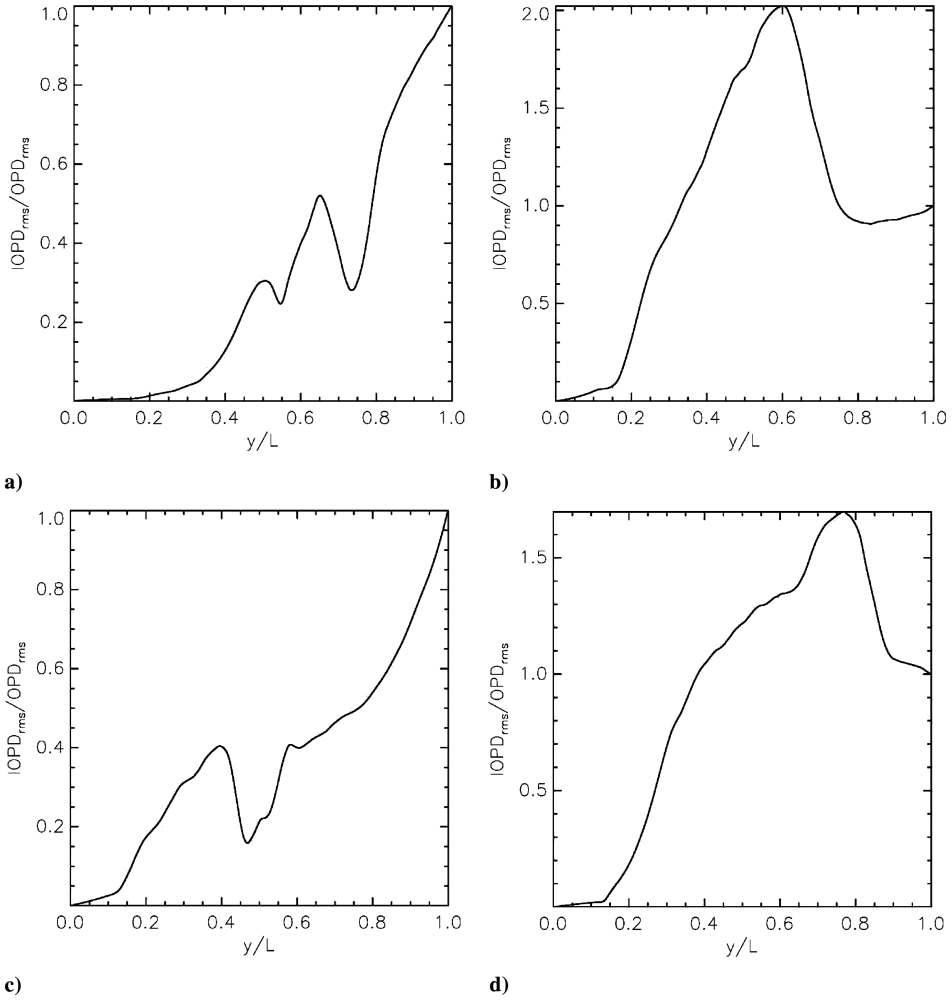

Fig. 11 Associated $IOPD_{rms}$ plots of the quarter-width laser aperture images in Fig. 10.

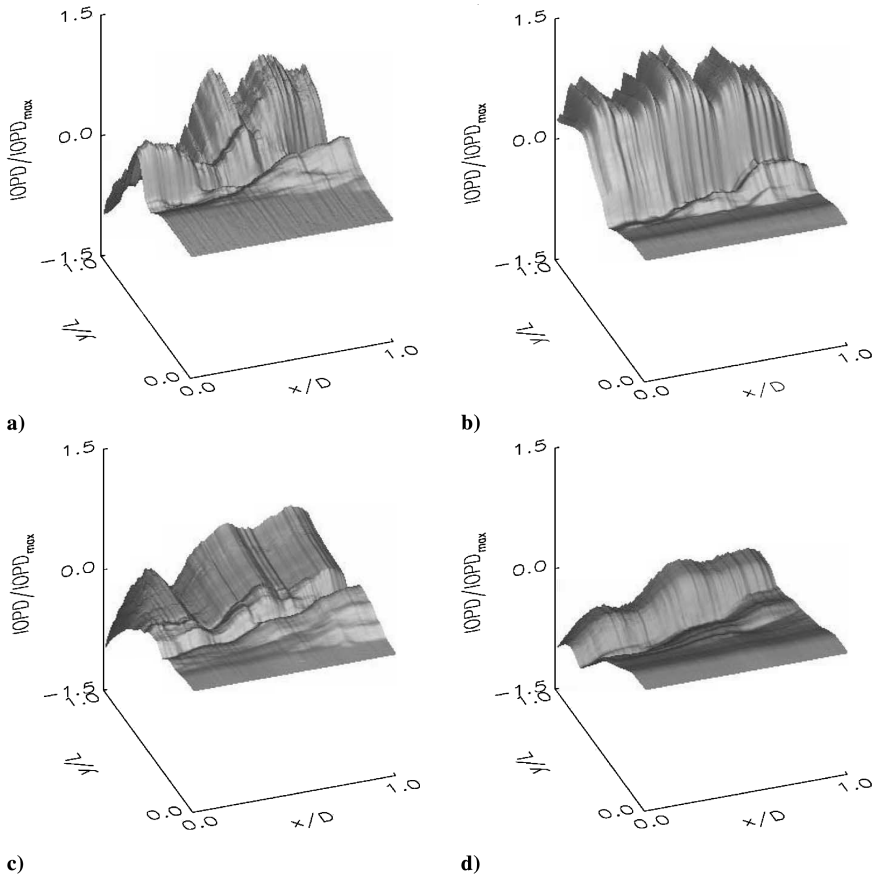

Fig. 12 Associated IOPD surface plots of the quarter-width laser aperture images in Fig. 10.

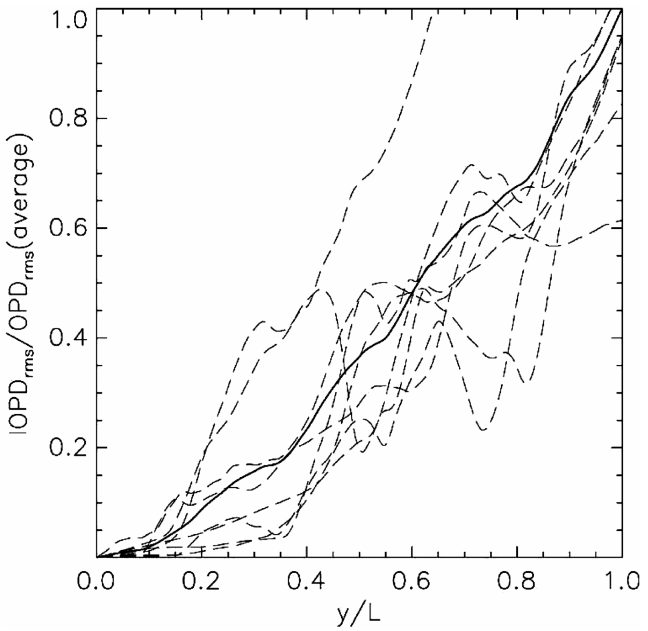

Fig. 13 The IOPD$_{rms}$ profiles depicted in this plot are derived from beams with quarter-width aperture sizes. The dotted curves represent several IOPD$_{rms}$ plots of laser beams propagated through different shear layers. Multiple occurrences of partial reductions are evident, indicating frequent nonmonotonic behavior. The solid curve represents the average IOPD$_{rms}$ behavior. It can be noted that the average behavior of the IOPD$_{rms}$ shows a purely monotonic increase in IOPD$_{rms}$ from the beginning to the end of the propagation path through the turbulent shear layer.

distorted and then, through interactions with various refractive-index gradients, corrects some of the distortions before it leaves the shear layer. Figure 7a also shows evidence that there can be multiple partial reductions in the IOPD$_{rms}$ value as the beam propagates through the shear layer. This further implies that there are refractive-index gradients that, due to position and shape of the incoming wave front, can increase or decrease the beam distortions. Figure 9 shows the associated IOPD surface plots of the images in Fig. 7. As with the other surface plots, the distortions are not necessarily monotonic through the shear layer.

Further reducing the beam aperture size [e.g., at a quarter-width ($D = L/4$)] in relation to the shear-layer large scale suggests that the nonmonotonicity can become more pronounced. Figure 10 shows four quarter-width image strips of turbulent shear layers. Each of the images are sections of different shear layers to ensure uncorrelated results. Computationally propagating beams through these images yields the results found in Figs. 11 and 12. Each of the associated IOPD$_{rms}$ images in Fig. 11 show very different profiles. Figure 11a shows two very distinct partial reductions in the IOPD$_{rms}$ value as the beam propagates through the shear layer. Figures 11b and 11d both show a maximum in the IOPD$_{rms}$ value that does not correspond with the end of the shear layer. Figure 11c shows a very notable decrease in the IOPD$_{rms}$ approximately halfway through the shear layer. Figure 12 shows the associated IOPD surface plots of the wave front as they propagate through these shear layers.

Figure 13 shows an ensemble average of multiple IOPD$_{rms}$ profiles in uncorrelated quarter segments of the turbulent fields. Whereas many of the quarter segments produced strong nonmonotonic behavior, the average of the IOPD$_{rms}$ values shows a purely monotonic behavior as expected. In general, turbulent shear layers are highly dynamic, and at certain times, a shear layer can have refractive gradients positioned in such a way that the incoming wave front will correct itself as opposed to getting more distorted. However, on average, the wave front distortion will increase as a beam enters the shear layer. It is not surprising that, despite all the strong nonmonotonic behavior observed by individual shear-layer

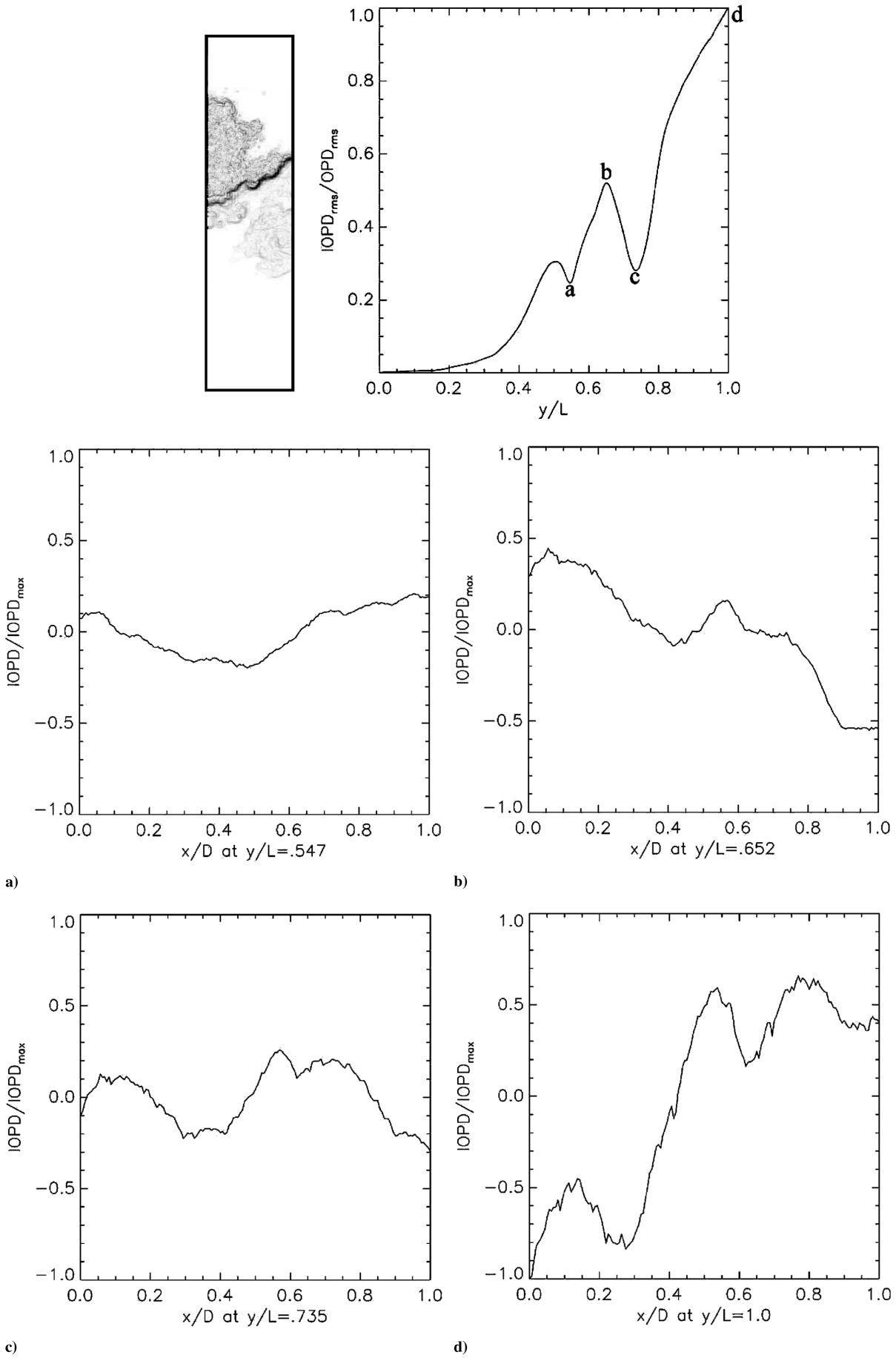

Fig. 14 Examination of Fig. 10a with associated refractive-index gradient field (top left), $IOPD_{rms}$ plot (top right), and IOPD plots at four specific points of interest.

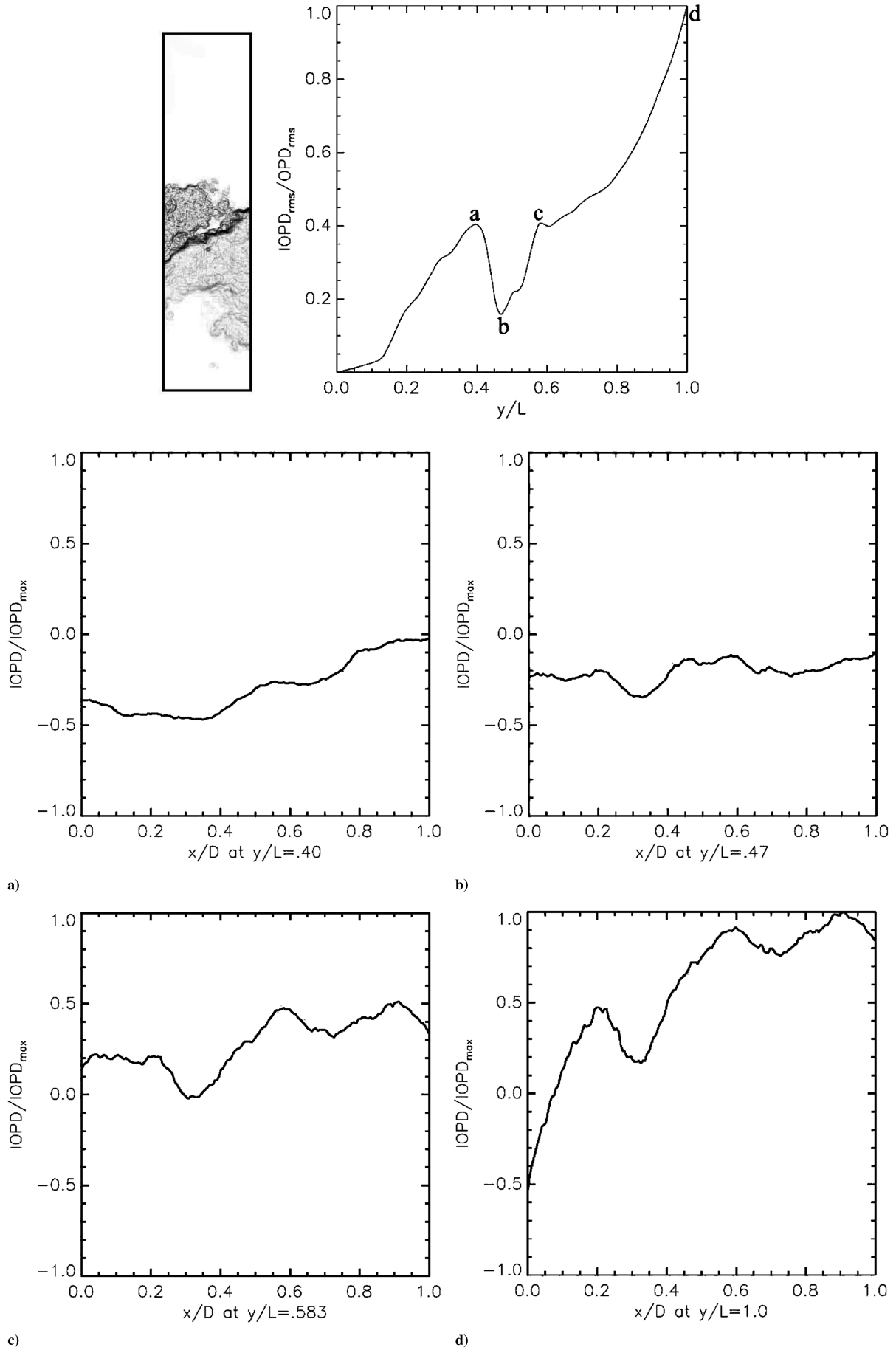

Fig. 15 Examination of Fig. 10c with associated refractive-index gradient field (top left), $IOPD_{rms}$ plot (top right), and IOPD plots at four specific points of interest.

segments, the average of those shows an almost linear monotonic behavior in the $IOPD_{rms}$.

To help identify how the refractive-index boundaries affect the shear layer, Figs. 14 and 15 show two examples of $IOPD_{rms}$ plots of quarter segments with the associated gradient fields. In addition, IOPD plots of noteworthy locations in the $IOPD_{rms}$ plots are shown to visually identify how the wave fronts get more or less distorted as they propagate through the flowfield. Figure 14 shows two partial reductions in the $IOPD_{rms}$ value, which appear to be correlated with the propagation of the wave front through the locally thin high-gradient refractive interface. Inspection of the IOPD plots provides insight into the turbulence-induced mechanism for partial reduction of the aberrations. For example, in Fig. 14, it can be seen that at point b, the wave front is highly distorted. however, after passing the refractive-index boundary, the wave front has peak values closer to each other, making it less distorted at point c. A very similar pattern can be seen in Fig. 15, in which a high-gradient refractive-index boundary creates a steep decrease in $IOPD_{rms}$ value. This decrease is associated with a more visually ordered IOPD (point b) wave front when compared with points a and c. In both figures, point d shows a relatively more distorted wave front as the beam passes through the shear layer. In addition, one can notice the high correlation between the location of the high-gradient refractive-index boundaries and the observed decrease in the $IOPD_{rms}$ value. This correlation reinforces the notion that the structure and orientation of these refractive-index interfaces is a key aspect of the turbulence-induced mechanism responsible for the multiple partial reductions in laser aberrations. It is a valuable, and perhaps surprising, observation that the beam can become partially undistorted during propagation in the flow due to the nature of the turbulent refractive-index interfaces, in particular, the high-gradient interfaces. In contrast, the ensemble-averaged behavior does not show any partial reduction in the aberrations. However, for practical applications, it is the individual-realization behavior or instantaneous flow structure that is crucial. Thus, the present findings of partial reductions in aberrations, induced directly by the turbulent interfacial behavior, can be expected to be valuable for practical and basic aero-optical problems.

IV. Conclusions

Aero-optical interactions along laser beam propagation paths have been examined on the basis of direct imaging of the refractive-index field in turbulent compressible separated shear layers. The interaction optical path difference and its associated root-mean-square value have been investigated as functions of propagation distance along the laser beam direction as well as functions of the laser aperture size. Evidence of nonmonotonic behavior of the $IOPD_{rms}$ as a function of propagation distance in the flow is observed for individual realizations. The average case supports the conclusion that generally monotonic behavior is observed in shear-layer flow. The extent of this behavior depends on the laser aperture size in relation to the large scales of the flow. These observations of nonmonotonic behavior suggest the presence of a turbulence-induced mechanism for partial reductions in the beam aberrations, which are related to physical and geometrical properties of the refractive-index turbulent interfaces. Refractive-index gradient images indicate that the locally thin high-gradient interfaces are able to produce this nonmonotonic behavior. These local interfaces and the associated aero-optical interactions across them therefore contribute partial reductions in the $IOPD_{rms}$ value of the propagating wave front. In general, the occurrences and extents of these interactions can be expected to depend on the orientation of, and gradients across, these interfaces. Understanding how the refractive-index boundaries affect the wave front can aid in reducing aero-optical distortion in directed-energy systems operating in highly turbulent conditions. Flow-forcing techniques can be used to create specific turbulent flowfields with suitable refractive-index gradients that can interact with a wave front (or predistorted wave front generated by adaptive optics techniques) to allow for optimally undistorted wave fronts to emerge from the flowfield. These resulting wave fronts can then be used in various directed-energy applications.

Acknowledgments

This research is part of a program on turbulence and the dynamics of flows. We are grateful for the support from the U.S. Air Force Office of Scientific Research by Program Manager Lt. Col. Rhett Jefferies. We are thankful to R. Aguirre, who developed the facility and conducted prior related work, as well as P. Garcia and J. Nathman for their contributions. We are grateful to the Referees for their insightful suggestions.

References

[1] Jumper, E. J., and Fitzgerald, E. J., "Recent Advances in Aero-Optics," *Progress in Aerospace Sciences*, Vol. 37, No. 3, Apr. 2001, pp. 299–339.

[2] Catrakis, H. J., "Turbulence and the Dynamics of Fluid Interfaces with Applications to Mixing and Aero-Optics," *Recent Research Developments in Fluid Dynamics*, Vol. 5, edited by N. Ashgriz and R. Anthony, Transworld Research Network, Kerala, India, 2004, pp. 115–158.

[3] Liepmann, H. W., "Deflection and Diffusion of a Light Ray Passing Through a Boundary Layer," Douglas Aircraft Co., Rept. SM-14397, Santa Monica, CA, May 1952.

[4] Kyrazis, D., "Optical Degradation by Turbulent Free Shear Layers," *Optical Diagnostics in Fluid and Thermal Flow*, edited by S. S. Cha and J. D. Trolinger, SPIE, Orlando, FL, 1993, pp. 170–181.

[5] Dimotakis, P. E., Catrakis, H. J., and Fourguette, D. C. L., "Flow Structure and Optical Beam Propagation in High-Reynolds-Number Gas-Phase Shear Layers and Jets," *Journal of Fluid Mechanics*, Vol. 433, June 2001, pp. 105–134.

[6] Jones, M., and Bender, E. E., "CFD-Based Computer Simulation of Optical Turbulence Through Aircraft Flowfields and Wakes," AIAA 32rd Plasmadynamics and Lasers Conference, Anaheim, CA, AIAA Paper 2001-2798, June 2001.

[7] Tromeur, E., Garnier, E., Sagaut, P., and Basdevant, C., "Large Eddy Simulations of Aero-Optical Effects in a Turbulent Boundary Layer," *Journal of Turbulence*, Vol. 4, No. 5, 2003, pp. 1–22.

[8] Fitzgerald, E. J., and Jumper, E. J., "The Optical Distortion Mechanism in a Nearly Incompressible Free Shear Layer," *Journal of Fluid Mechanics*, Vol. 512, July 2004, pp. 153–189.

[9] Catrakis, H. J., and Aguirre, R. C., "New Interfacial Fluid Thickness Approach in Aero-Optics with Applications to Compressible Turbulence," *AIAA Journal*, Vol. 42, No. 10, 2004, pp. 1973–1981.

[10] Aguirre, R. C., and Catrakis, H. J., "Aero-Optical Wave Fronts and Scale-Local Characterization in Large-Reynolds-Number Compressible Turbulence," *AIAA Journal*, Vol. 42, No. 10, 2004, pp. 1982–1990.

[11] Moin, P., and Mahesh, K., "Direct Numerical Simulations: A Tool in Turbulence Research," *Annual Review of Fluid Mechanics*, Vol. 30, 1998, pp. 539–578.

[12] Meneveau, C., and Katz, J., "Scale-Invariance and Turbulence Models for Large-Eddy Simulation," *Annual Review of Fluid Mechanics*, Vol. 32, 2000, pp. 1–32.

[13] Truman, C. R., and Lee, M. J., "Effects of Organized Turbulence Structures on the Phase Distortion in a Coherent Optical Beam Propagating Through a Turbulent Shear Flow," *Physics of Fluids A*, Vol. 2, No. 5, 1990, pp. 851–857.

[14] Hentschel, H. G. E., and Procaccia, I., "Passive Scalar Fluctuations in Intermittent Turbulence with Applications to Wave Propagation," *Physical Review A*, Vol. 28, No. 1, 1983, pp. 417–426.

[15] Schwartz, C., Baum, G., and Ribak, E. N., "Turbulence-Degraded Wave Fronts as Fractal Surfaces," *Journal of the Optical Society of America*, Vol. 11, No. 1, 1994, pp. 444–451.

[16] Morris, S., and Foss, J., "Turbulent Boundary Layer to Single-Stream Shear Layer: The Transition Region," *Journal of Fluid Mechanics*, Vol. 494, Nov. 2003, pp. 187–221.

[17] Stanek, M., Sinha, N., Seiner, J., Pearce, B., and Jones, M., "High Frequency Flow Control: Suppression of Aero-Optics in Tactical Directed Energy Beam Propagation and the Birth of a New Model (Part 1)," AIAA 33rd Plasmadynamics and Lasers Conference, Maui, HA, AIAA Paper 2002-2272, June 2002.

[18] Thurber, M. C., and Hanson, R. K., "Pressure and Composition Dependences of Acetone Laser-Induced Fluorescence with Excitation at 248, 266, and 308 nm," *Applied Physics B (Lasers and Optics)*, Vol. 69, No. 3, 1999, pp. 229–240.

[19] Catrakis, H. J., Aguirre, R. C., Ruiz-Plancarte, J., Thayne, R. D., McDonald, B. A., and Hearn, J. W., "Large-Scale Dynamics in Turbulent Mixing and the Three-Dimensional Space-Time Behaviour of Outer Fluid Interfaces," *Journal of Fluid Mechanics*, Vol. 471,

Nov. 2002, pp. 381–408.
[20] Mani, A., Wang, M., and Moin, P., "Statistical Description of the Free-Space Propagation of Highly Aberrated Optical Beams," *Journal of the Optical Society of America*, Vol. 23, No. 12, pp. 3027–3035.
[21] Elghobashi, S. E., and Wassel, A. T., "The Effect of Turbulent Heat Transfer on the Propagation of an Optical Beam Across Supersonic Boundary/Shear Layers," *International Journal of Heat and Mass Transfer*, Vol. 23, Sept. 1980, pp. 1229–1241.
[22] Yahel, R. Z., "Turbulence Effects on High Energy Laser Beam Propagation in the Atmosphere," *Applied Optics*, Vol. 29, No. 21, 1990, pp. 3088–3095.
[23] Liepmann, H. W., "Aspects of the Turbulence Problem," Parts 1, 2, 3, *Zeitschrift für angewandte Mathematik und Physik*, Vol. 3, No. 5, 1952, pp. 321–342.
[24] Born, M., and Wolf, E., *Principles of Optics: Electromagnetic Theory of Propagation, Interference and Diffraction of Light*, 7th ed., Cambridge Univ. Press, New York, 1999.

J. Gore
Associate Editor